Novel PWM Schemes With Multi SVPWM of Sensorless IPMSM Drives for Reducing Current Ripple

Minglei Gu, Satoshi Ogasawara, *Senior Member, IEEE*, and Masatsugu Takemoto, *Member, IEEE*

***Abstract*—This paper proposes novel pulsewidth modulation (PWM) schemes for multi-space-vector pulsewidth modulation (MSVPWM), which is used in position sensorless control of interior permanent-magnet synchronous motor drives. The estimation of the rotor position is based on magnetic saliency and employs high-frequency components of voltage and current, which are excited by MSVPWM. The difference between the instantaneously applied voltage vector and the reference voltage vector causes current ripple. Since six or four voltage vectors are generated during a PWM period, the sequences of the error voltage vectors lead to different types of current ripples. In this paper, the proposed MSVPWM schemes employ six sequences for zero-/low-speed operation and 24 sequences for high-speed operation to reduce line current ripple. Experimental results confirm that the proposed MSVPWM schemes lead to significant reduction in harmonic current while maintaining high performance of sensorless estimation.**

***Index Terms*—Harmonic current, interior permanent-magnet synchronous machine (IPMSM), magnetic saliency, multi-space-vector pulsewidth modulation (MSVPWM), position estimation, sensorless, switching sequence.**

I. Introduction

INTERIOR permanent-magnet synchronous machines (IPMSMs) are used in increasingly diverse industrial, household, and automotive applications. Their advantages include reduced motor loss, higher power density, lower rotor inertia, and greater robustness of the rotor [1]–[4]. Due to the high cost and large space requirements of position sensors in such machines, sensorless IPMSM control systems are expected to be more competitive. In such systems, it is possible to estimate the rotor position signal from stator terminal voltages and currents [5].

Since the counter electromotive force (CEMF) becomes unobservable when the rotor is running below a certain speed, position estimation based on CEMF becomes impossible at low speed, particularly at startup [6]–[12].

Position estimation based on the saliency effect is the only way to estimate the position of the rotor when it is stationary or rotating in low-speed operation. This estimation method can be categorized as follows.

Manuscript received October 28, 2013; revised April 21, 2015; accepted October 28, 2015. Date of publication November 19, 2015; date of current version March 25, 2016. Recommended for publication by Associate Editor R. Kennel.

The authors are with the Department of Information Science and Technology, Hokkaido University, Sapporo 060-0808, Japan (e-mail: ko@sfc.ssi.ist.hokudai.ac.jp; oga@ist.hokudai.ac.jp; takemoto@ist.hokudai.ac.jp).

Color versions of one or more of the figures in this paper are available online at http://ieeexplore.ieee.org.

Digital Object Identifier 10.1109/TPEL.2015.2500364

1) *Position Estimation Based on High-Frequency (HF) Signal Injection:* An HF signal, which can be a rotating voltage vector, an alternating voltage vector or a pulse pattern, is injected at the $\alpha\beta$ or *dq* components [13]–[22]. The response signal is usually evaluated from the HF current, current derivative or HF voltage. This method is possibly the most commonly used for position estimation. However, signal extraction with filter which is used for distinguishing the HF response from the controlled current, tends to degrade the time response of vector control.
2) *Position Estimation Based on Zero-Sequence Component:* The advantages of this method are high vector control performance and simple estimation process. Since the neutral point of the motor must be accessible for exciting the zero-sequence component, a modified stator winding structure is needed, which is not suitable for general industrial applications [23].
3) *Position Estimation Based on Modified Pulse Width Modulation (PWM):* With this kind of methods, a real-time position can be estimated at low and zero speed [24]–[29]. In [24] and [25], multi-space-vector pulsewidth modulation (MSVPWM) is presented. The HF components of voltage and current produced by MSVPWM are used. The excitation is generated by six or four voltage vectors and the response of HF component is obtained by a simple current sampling device. In [28], two voltage vectors that are opposite to the nonzero vectors of the conventional space vector pulsewidth modulation (SVPWM), are used to increase the excitation time when the average output voltage vector is small. In [29], a pair of test vectors that is equal and opposite, is imposed during the null period of the conventional SVPWM. In addition, [28], [29] require *di*/*dt* sensors to measure response signals.

Since the conventional SVPWM is possibly the best among all the PWM techniques, modified PWMs must compromise PWM performance in order to make the magnetic saliency effect available. One disadvantage is that the undesired switching sequences boost the harmonic current.

In [30] and [31], hybrid SVPWM schemes for reduced current ripple are discussed. Hua *et al.* [32] employed the opposite switching vector to reduce the additional current deviation caused by the modified PWM in [28]. Since six active voltage vectors are generated by MSVPWM during a PWM period, the output sequences of the multiple error voltage vectors lead to the different kinds of current ripple. This paper analyzes *dq*-axis HF current ripple during a PWM period for the various possible

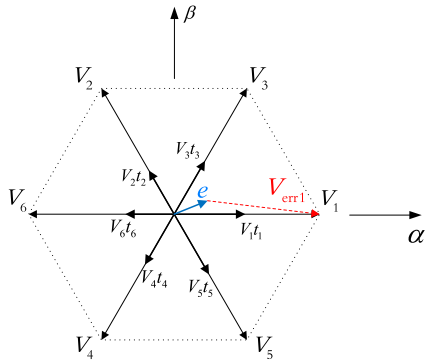

Fig. 1. Voltage vectors of inverter output.

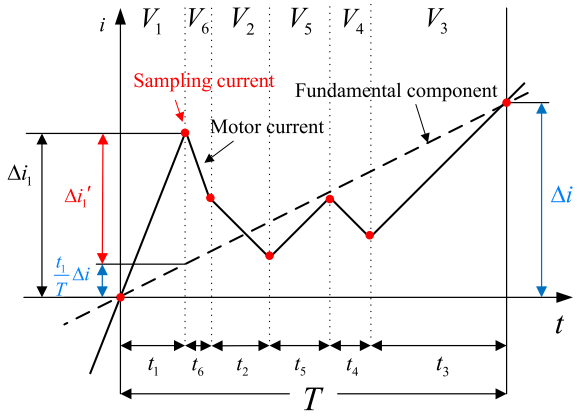

Fig. 2. Waveform of the motor current.

MSVPWM schemes. Taking various salience rate and output voltage vector into consideration, three types of optimization MSVPWM schemes for reducing HF current ripple are proposed. Consequently, the harmonic loss and the efficiency of the system can be improved. Experimental results at low-speed, $i_d = 0$ operation confirm that the proposed MSVPWM schemes lead to a significant reduction in harmonic current while maintaining high performance of sensorless position estimation. The most effective MSVPWM schemes can be determined in real time with the help of online inductance estimation.

II. Principles of Position Estimation

A. HF Model of IPMSM

An IPMSM can be modeled with a stationary reference frame $\alpha\beta$ as follows:

$$\begin{bmatrix} v_\alpha \\ v_\beta \end{bmatrix} = \begin{bmatrix} r & 0 \\ 0 & r \end{bmatrix} \begin{bmatrix} i_\alpha \\ i_\beta \end{bmatrix} + \begin{bmatrix} L_0 + L_1 \cos 2\theta & L_1 \sin 2\theta \\ L_1 \sin 2\theta & L_0 - L_1 \cos 2\theta \end{bmatrix} \times \begin{bmatrix} \dfrac{di_\alpha}{\mathrm{dt}} \\ \dfrac{di_\beta}{\mathrm{dt}} \end{bmatrix} + \frac{d\theta}{\mathrm{dt}} \left(2L_1 \begin{bmatrix} -\sin 2\theta & \cos 2\theta \\ \cos 2\theta & \sin 2\theta \end{bmatrix} \begin{bmatrix} i_\alpha \\ i_\beta \end{bmatrix} + \psi_f \begin{bmatrix} -\sin\theta \\ \cos\theta \end{bmatrix} \right) \tag{1}$$

$$L_0 = \frac{L_d + L_q}{2}, \tag{2}$$

$$L_1 = \frac{L_d - L_q}{2} \tag{3}$$

where v_α and v_β are the stator voltages, and i_α and i_β are the stator currents in the stationary reference frame $\alpha\beta$; r is the motor resistance; and ψ_f is the permanent magnet's flux linkage. L_d and L_q are the direct and quadrature inductance in the rotor-oriented reference frame dq.

Since CEMF is a fundamental component, the HF component of the resistive voltage drop $r\boldsymbol{i}'$ is negligible. (1) can be simplified by writing the HF component as

$$\boldsymbol{v}' = \boldsymbol{L}\frac{di'}{dt}. \tag{4}$$

Here, $\boldsymbol{v}'$, $\boldsymbol{i}'$ denote the harmonic components, $\boldsymbol{L}$ is the inductance matrix of (1)

$$\boldsymbol{L} = \begin{bmatrix} L_0 + L_1 \cos 2\theta & L_1 \sin 2\theta \\ L_1 \sin 2\theta & L_0 - L_1 \cos 2\theta \end{bmatrix} = \begin{bmatrix} L_\alpha(\theta) & L_{\alpha\beta}(\theta) \\ L_{\beta\alpha}(\theta) & L_\beta(\theta) \end{bmatrix}. \tag{5}$$

The aforementioned equation indicates that with the help of the HF components of the motor voltage and current vectors, the inductance matrix $\boldsymbol{L}$ can be estimated. From this, the rotor position 2θ can be obtained with

$$2\theta = \tan^{-1}\frac{L_{\alpha\beta} + L_{\beta\alpha}}{L_\alpha - L_\beta}. \tag{6}$$

B. Extraction of High-Frequency Components

In a three-phase voltage-source inverter, six active space vectors $\boldsymbol{V}_{1-6}$ and two zero space vectors $\boldsymbol{V}_{0,7}$ can be generated, as shown in Fig. 1. The average voltage vector $\boldsymbol{e}$ can be regarded as the fundamental voltage vector. Therefore, the HF voltage vector $\boldsymbol{V}_k{}'$ is equal to the difference between the inverter output voltage vector $\boldsymbol{V}_k$ and the average output voltage vector $\boldsymbol{e}$

$$\boldsymbol{V}'_{\boldsymbol{k}} = \boldsymbol{V}_{\boldsymbol{k}} - \boldsymbol{e}. \tag{7}$$

Fig. 2 shows the waveform of the motor current when $\boldsymbol{V}_{1-6}$ are used during a modulation period. It can be assumed that the fundamental component varies linearly during a modulation period T. The current variation of an HF component $\boldsymbol{\Delta}i_k{}'$ during t_k is

$$\Delta\boldsymbol{i}'_{\boldsymbol{k}} = \Delta\boldsymbol{i}_{\boldsymbol{k}} - \frac{t_k}{T}\Delta\boldsymbol{i} \tag{8}$$

$$\Delta\boldsymbol{i} = \sum_{k=0}^{7}\Delta\boldsymbol{i}_{\boldsymbol{k}}. \tag{9}$$

Here, $\boldsymbol{\Delta}i_k$ is the current response of inverter output voltage vector $\boldsymbol{V}_k$, and $\Delta\boldsymbol{i}$ is the response current of the average output voltage vector $\boldsymbol{e}$.

The HF voltage vector $\boldsymbol{V}'_k$ can be determined incidentally by space vector modulation algorithm. The HF current $\Delta\boldsymbol{i}'_k$ is obtained by a simple current sampling device [25]. Since the HF current component can be extracted in real time, both the

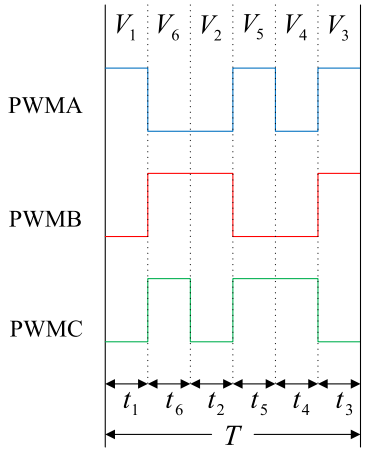

Fig. 3. Conventional MSVPWM scheme.

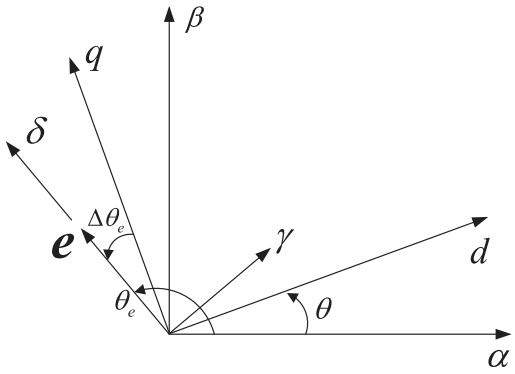

Fig. 4. Definition of the $\gamma\delta$-axis, dq-axis and $\alpha\beta$-axis of the error voltage vectors.

position and the inductances can be estimated instantly in the next control cycle.

III. MSVPWM

The conventional SVPWM is possibly the best among all the PWM techniques, however, when the magnitude of the average output voltage vector $\boldsymbol{e}$ is near zero or its vector angle is close to that of $\boldsymbol{V}_k$, the HF excitation is too small to measure HF current response, consequently, position estimation cannot work perfectly in SVPWM.

To eliminate this drawback of SVPWM, an MSVPWM scheme is adopted. To increase the efficiency of the HF effect at the arbitrary average output voltage vector $\boldsymbol{e}$, all eight voltage vectors can be used in MSVPWM. The average voltage vector $\boldsymbol{e}$ during a modulation period can be expressed in general form as

$$\boldsymbol{e} = \sum_{k=0}^{7} s_k \zeta_k \boldsymbol{V}_k \tag{10}$$

$$\sum_{k=0}^{7} s_k \zeta_k = 1. \tag{11}$$

Here, a switch selector s_k, which takes a value of 1 or 0, indicates whether $\boldsymbol{V}_k$ is selected as an output vector during the modulation period T. ζ_k is the ratio of the action time t_k to the modulation period T. (10) can be expressed in matrix form in the stationary reference frame $\alpha\beta$ as follows:

$$\begin{bmatrix} e_\alpha \\ e_\beta \\ 1 \end{bmatrix} = \begin{bmatrix} s_0 V_{0\alpha} & s_1 V_{1\alpha} & \cdots & s_7 V_{7\alpha} \\ s_0 V_{0\beta} & s_1 V_{1\beta} & \cdots & s_7 V_{7\beta} \\ s_0 & s_1 & \cdots & s_7 \end{bmatrix} \begin{bmatrix} \zeta_0 \\ \zeta_1 \\ \vdots \\ \zeta_7 \end{bmatrix}. \tag{12}$$

No general solution to (12) exists because the number of unknown variables is greater than the number of equations. Here, a right pseudoinverse matrix is applied to obtain the least-squares solution of the sum of ζ_k^2, which is defined as

$$\boldsymbol{F}^{\mathrm{RM}} = \boldsymbol{F}^T (\mathbf{F}\mathbf{F}^T)^{-1} \tag{13}$$

such that the magnitude of the average output voltage vector $\boldsymbol{e}$ can be extended during the same modulation period T

$$\begin{bmatrix} \zeta_0 \\ \zeta_1 \\ \vdots \\ \zeta_7 \end{bmatrix} = \begin{bmatrix} s_0 V_{0\alpha} & s_1 V_{1\alpha} & \cdots & s_7 V_{7\alpha} \\ s_0 V_{0\beta} & s_1 V_{1\beta} & \cdots & s_7 V_{7\beta} \\ s_0 & s_1 & \cdots & s_7 \end{bmatrix}^{\mathrm{RM}} \begin{bmatrix} e_\alpha \\ e_\beta \\ 1 \end{bmatrix}. \tag{14}$$

Fig. 3 shows the conventional MSVPWM scheme with s_0, $s_7 = 0$, and $s_{1\sim6} = 1$, which means all of the six nonzero-voltage vectors $\boldsymbol{V}_{1-6}$ are selected and the two zero-voltage vectors $\boldsymbol{V}_{0,7}$ are ignored. In this case, (14) can be rewritten as (15). Here, V_{dc} is the dc-link voltage of the inverter

$$\begin{bmatrix} \zeta_0 & \zeta_4 \\ \zeta_1 & \zeta_5 \\ \zeta_2 & \zeta_6 \\ \zeta_3 & \zeta_7 \end{bmatrix} = \begin{bmatrix} 0 & -\dfrac{\sqrt{6}e_\alpha}{3V_{\mathrm{dc}}} - \dfrac{\sqrt{2}e_\beta}{V_{\mathrm{dc}}} + \dfrac{1}{6} \\ \dfrac{\sqrt{6}e_\alpha}{6V_{\mathrm{dc}}} + \dfrac{1}{6} & \dfrac{\sqrt{6}e_\alpha}{3V_{\mathrm{dc}}} - \dfrac{\sqrt{2}e_\beta}{V_{\mathrm{dc}}} + \dfrac{1}{6} \\ -\dfrac{\sqrt{6}e_\alpha}{3V_{\mathrm{dc}}} + \dfrac{\sqrt{2}e_\beta}{V_{\mathrm{dc}}} + \dfrac{1}{6} & -\dfrac{\sqrt{6}e_\alpha}{6V_{\mathrm{dc}}} + \dfrac{1}{6} \\ \dfrac{\sqrt{6}e_\alpha}{3V_{\mathrm{dc}}} + \dfrac{\sqrt{2}e_\beta}{V_{\mathrm{dc}}} + \dfrac{1}{6} & 0 \end{bmatrix}. \tag{15}$$

To maintain the applicability of this algorithm, $0 < \zeta_{1-6} < 1$ is needed. This imposes the value of $e_m \big/ (\sqrt{2/3}V_{\mathrm{dc}})$ must be less than 1/2 for a sinusoidal output. Here, e_m is the magnitude of the average output voltage vector $\boldsymbol{e}$. This MSVPWM scheme is suitable for startup and low-speed operation. Another MSVPWM scheme suitable for middle and high-speed operation is described in Section V-E.

IV. Analysis of Current Ripple During a Modulation Period

Note that the HF voltage component $\boldsymbol{V}_k{}'$ can also be regarded as the error voltage vector $\boldsymbol{V}_{\mathrm{err}k}$, which induce ripples in the line currents of the motor. According to (7), the $\alpha\beta$-axis components of the error voltage vector $\boldsymbol{V}_{\mathrm{err}k\alpha}$ and $\boldsymbol{V}_{\mathrm{err}k\beta}$ are expressed as follows: (16) and (17) shown at bottom of the next page.

Here, θ_e is the angle of the average output voltage vector $\boldsymbol{e}$ in the stationary reference frame $\alpha\beta$.

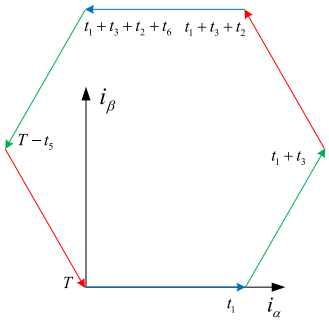

Fig. 5. Trajectory of the error current of the counterclockwise sequence $(V_1V_3V_2V_6V_4V_5)$.

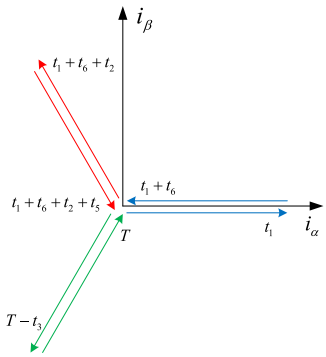

Fig. 6. Trajectory of the error current of the conventional sequence $(V_1V_6V_2V_5V_4V_3)$.

In order to make a quantitative analysis of the current ripple with the influence of saliency ratio, the rotational reference frame $\gamma\delta$ is defined. The δ-axis is aligned with the output voltage vector $\boldsymbol{e}$, and the γ-axis lags behind the δ-axis by 90°, as shown in Fig. 4. The angle between q-axis and δ-axis is defined as $\Delta\theta_e$. The dq-axis components of the error voltage vectors $V_{\mathrm{err}kd}$ and $V_{\mathrm{err}kq}$ are expressed as follows: (18) and (19) shown at bottom of the page.

It is assumed that current ripples change linearly, with a slope changing immediately at the moment of switching. Then, the instantaneous current ripple vector $\boldsymbol{i}_{\mathrm{ripple}}$ can be approximately expressed as follows:

$$i_{\mathrm{rippled}}(t) = \frac{\int_0^T V_{\mathrm{err}d}(t)dt}{L_d} \tag{20}$$

$$i_{\mathrm{rippleq}}(t) = \frac{\int_0^T V_{\mathrm{err}q}(t)dt}{L_q}. \tag{21}$$

Here, $i_{\mathrm{rippled}}(t)$ and $i_{\mathrm{rippleq}}(t)$ are the dq-axis components of the instantaneous current ripple, respectively.

The root mean square (RMS) of the dq-axis current ripples I_{rippled} and I_{rippleq} are defined as follows:

$$I^2_{\mathrm{rippled}} = \frac{\int_0^T i^2_{\mathrm{rippled}}(t)dt}{T} \tag{22}$$

$$I^2_{\mathrm{rippleq}} = \frac{\int_0^T i^2_{\mathrm{rippleq}}(t)dt}{T}. \tag{23}$$

$$\begin{bmatrix} V_{\mathrm{err}1\alpha} & V_{\mathrm{err}4\alpha} \\ V_{\mathrm{err}2\alpha} & V_{\mathrm{err}5\alpha} \\ V_{\mathrm{err}3\alpha} & V_{\mathrm{err}6\alpha} \end{bmatrix} = \begin{bmatrix} \frac{\sqrt{6}}{3}V_{\mathrm{dc}} - e_m\cos\theta_e & -\frac{\sqrt{6}}{6}V_{\mathrm{dc}} - e_m\cos\theta_e \\ -\frac{\sqrt{6}}{6}V_{\mathrm{dc}} - e_m\cos\theta_e & \frac{\sqrt{6}}{6}V_{\mathrm{dc}} - e_m\cos\theta_e \\ \frac{\sqrt{6}}{6}V_{\mathrm{dc}} - e_m\cos\theta_e & -\frac{\sqrt{6}}{3}V_{\mathrm{dc}} - e_m\cos\theta_e \end{bmatrix} \tag{16}$$

$$\begin{bmatrix} V_{\mathrm{err}1\beta} & V_{\mathrm{err}4\beta} \\ V_{\mathrm{err}2\beta} & V_{\mathrm{err}5\beta} \\ V_{\mathrm{err}3\beta} & V_{\mathrm{err}6\beta} \end{bmatrix} = \begin{bmatrix} -e_m\sin\theta_e & -\frac{\sqrt{2}}{2}V_{\mathrm{dc}} - e_m\sin\theta_e \\ \frac{\sqrt{2}}{2}V_{\mathrm{dc}} - e_m\sin\theta_e & -\frac{\sqrt{2}}{2}V_{\mathrm{dc}} - e_m\sin\theta_e \\ \frac{\sqrt{2}}{2}V_{\mathrm{dc}} - e_m\sin\theta_e & -e_m\sin\theta_e \end{bmatrix}. \tag{17}$$

$$\begin{bmatrix} V_{\mathrm{err}1d} V_{\mathrm{err}4d} \\ V_{\mathrm{err}2d} V_{\mathrm{err}5d} \\ V_{\mathrm{err}3d} V_{\mathrm{err}6d} \end{bmatrix} = \begin{bmatrix} \sqrt{\frac{2}{3}}V_{\mathrm{dc}}\cos\theta + e_m\sin\Delta\theta_e & \sqrt{\frac{2}{3}}V_{\mathrm{dc}}\cos\left(\theta+\frac{2\pi}{3}\right) + e_m\sin\Delta\theta_e \\ \sqrt{\frac{2}{3}}V_{\mathrm{dc}}\cos\left(\theta+\frac{4\pi}{3}\right) + e_m\sin\Delta\theta_e & \sqrt{\frac{2}{3}}V_{\mathrm{dc}}\cos\left(\theta+\frac{\pi}{3}\right) + e_m\sin\Delta\theta_e \\ \sqrt{\frac{2}{3}}V_{\mathrm{dc}}\cos\left(\theta+\frac{5\pi}{3}\right) + e_m\sin\Delta\theta_e & \sqrt{\frac{2}{3}}V_{\mathrm{dc}}\cos\left(\theta+\pi\right) + e_m\sin\Delta\theta_e \end{bmatrix} \tag{18}$$

$$\begin{bmatrix} V_{\mathrm{err}1q} & V_{\mathrm{err}4q} \\ V_{\mathrm{err}2q} & V_{\mathrm{err}5q} \\ V_{\mathrm{err}3q} & V_{\mathrm{err}6q} \end{bmatrix} = \begin{bmatrix} -\sqrt{\frac{2}{3}}V_{\mathrm{dc}}\sin\theta - e_m\cos\Delta\theta_e & -\sqrt{\frac{2}{3}}V_{\mathrm{dc}}\sin\left(\theta+\frac{2\pi}{3}\right) - e_m\cos\Delta\theta_e \\ -\sqrt{\frac{2}{3}}V_{\mathrm{dc}}\sin\left(\theta+\frac{4\pi}{3}\right) - e_m\cos\Delta\theta_e & -\sqrt{\frac{2}{3}}V_{\mathrm{dc}}\sin\left(\theta+\frac{\pi}{3}\right) - e_m\cos\Delta\theta_e \\ -\sqrt{\frac{2}{3}}V_{\mathrm{dc}}\sin\left(\theta+\frac{5\pi}{3}\right) - e_m\cos\Delta\theta_e & -\sqrt{\frac{2}{3}}V_{\mathrm{dc}}\sin\left(\theta+\pi\right) - e_m\cos\Delta\theta_e \end{bmatrix} \tag{19}$$

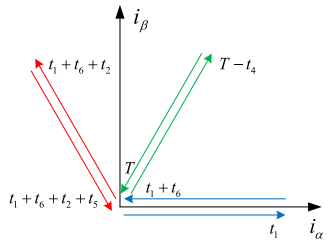

Fig. 7. Trajectory of the error current of the asymmetrical sequence $(V_1V_6V_2V_5V_3V_4)$.

The RMS of the total current ripple I_{ripple} can be regarded as the square root of the sum of (22) and (23)

$$I_{\text{ripple}}^2 = I_{\text{ripple}d}^2 + I_{\text{ripple}q}^2. \tag{24}$$

The minimum total current ripple I_{ripple} is taken as the optimized object to find out the most appropriate MSVPWM scheme during a single modulation period.

V. Sequence of MSVPWM

A. Constraints of MSVPWM

The behavior of the current ripple during a modulation period depends not only on the average output voltage vector $\boldsymbol{e}$, but also on the sequence of the time integrals of the components of the error voltage vectors. Since the voltage vectors V_{0-7} visually reflect the trajectory of the error current, the relationship between the MSVPWM schemes and the current ripples is discussed qualitatively in the stationary reference frame $\alpha\beta$ for a better understanding.

The MSVPWM schemes, which the action time ratios of the six active space vectors during a modulation period satisfies (10) to ensure voltage–time balance is theoretically valid. Therefore, there are $6! = 720$ possible valid schemes of vectors in MSVPWM. The total number of switching events during a modulation period is the lowest when the sequence is strictly clockwise or counterclockwise, however, in this case, strong current ripple is generated due to the excess time integrals of the error voltage vectors in the corresponding direction. The trajectory of the error current of the counterclockwise sequence $(V_1V_3V_2V_6V_4V_5)$ is shown in Fig. 5, where the magnitude of the average voltage vector $\boldsymbol{e}$ is set to zero.

To eliminate the aforementioned drawback, the authors' previous report [24] proposed the conventional MSVPWM scheme. A pair of voltage vectors with opposite orientation is employed to reduce the current ripple of the corresponding phase. In other words, (V_1V_6), (V_2V_5), (V_4V_3) are combined as fixed switching sequences in order to reduce the three-phase current ripple. The trajectory of the error current of the conventional sequence $(V_1V_6V_2V_5V_4V_3)$ is shown in Fig. 6, where the magnitude of the average voltage vector $\boldsymbol{e}$ is set to zero. The trajectory clearly starts from the origin and returns to the origin three times during a modulation period. Consequently, the time integrals of the error voltage vectors are closer to the origin and reduce the total current ripple.

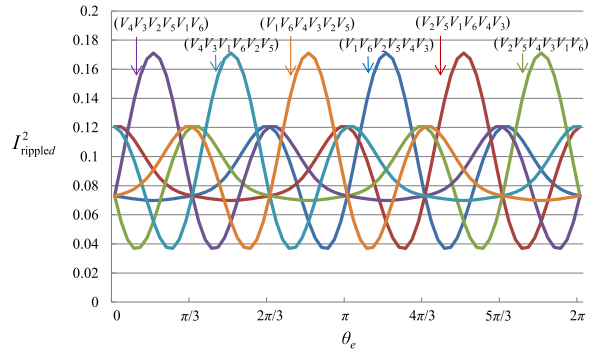

Fig. 8. Relation of the d-axis current ripple $I_{\text{ripple}d}$ with respect to the angle of the average output voltage vector when e_m is 0.4 of $\sqrt{2/3}V_{\text{dc}}$.

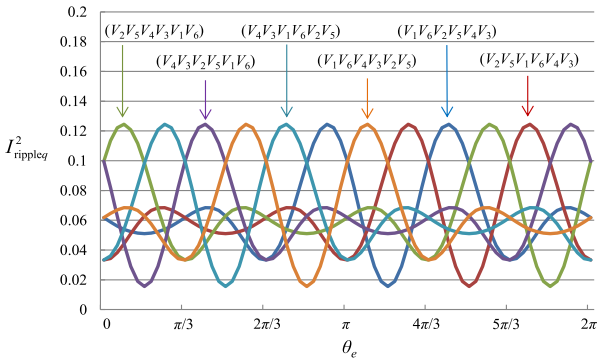

Fig. 9. Relation of the q-axis current ripple $I_{\text{ripple}q}$ with respect to the angle of the average output voltage vector when e_m is 0.4 of $\sqrt{2/3}V_{\text{dc}}$.

In addition, the symmetry of the three-phase error voltage vectors also contributes to the reduction of the current ripple. Fig. 7 shows the trajectory of the error current of the three-phase asymmetrical sequence $(V_1V_6V_2V_5V_3V_4)$. Since the switching sequence of phase C is (V_3V_4), the average time integrals of the all error voltage vectors are shifted away from origin, and an undesired current ripple occurs at 60°.

Note that there are five more MSVPWM schemes [$(V_2V_5V_1V_6V_4V_3)$, $(V_2V_5V_4V_3V_1V_6)$, $(V_4V_3V_2V_5V_1V_6)$, $(V_4V_3V_1V_6V_2V_5)$, and $(V_1V_6V_4V_3V_2V_5)$] that also satisfy the following principles:

1) employ three fixed pairs of switching sequences;
2) maintain symmetry of the three phases.

The analysis of the RMS of the current ripple generated during a modulation period in these MSVPWM schemes is presented in the following section.

B. Characteristics of RMS of Current Ripple

Taking the saliency ratio into account, current ripple is discussed quantitatively in the rotational reference frame dq to observe the influences of phase and magnitude of output voltage vector. In order to analyze the influence of voltage–time integrals of dq-axis components visually, L_d and L_q are both assumed to 20 mH extremely, $\Delta\theta_e$ is assumed to 0. In this section, V_{dc} is set to 200 V. The modulation period is set to 400 μs.

Figs. 8 and 9 show the current ripples $I_{\text{ripple}d}^2$ and $I_{\text{ripple}q}^2$ of the six available MSVPWM schemes with respect to the angle of the average output voltage vector $\boldsymbol{e}$ when e_m is set

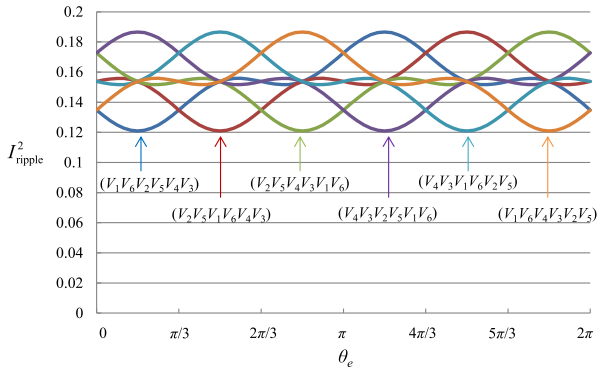

Fig. 10. Relation of the total current ripple with respect to the angle of the average output voltage vector when e_m is 0.4 of $\sqrt{2/3}V_{\text{dc}}$.

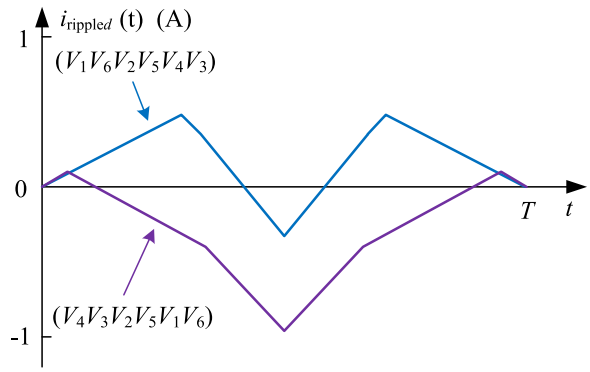

Fig. 11. d-axis instantaneous current ripple of sequences $(V_1V_6V_2V_5V_4V_3)$ and $(V_4V_3V_2V_5V_1V_6)$ at $\theta_e = 30°$.

to 0.4 of $\sqrt{2/3}V_{\text{dc}}$. In the conventional MSVPWM sequence $(V_1V_6V_2V_5V_4V_3)$, the d-axis current ripple reaches the minimum/maximum and the q-axis current ripple reaches the maximum/minimum at the same corresponding angles, respectively. For all six sequences, the characteristics of the individual current ripples are the same as that for $(V_1V_6V_2V_5V_4V_3)$, except for a 60° phase difference.

Fig. 10 shows the total current ripple I^2_{ripple}, which is the sum of I^2_{rippled} and I^2_{rippleq}. In the conventional MSVPWM sequence $(V_1V_6V_2V_5V_4V_3)$, the total current ripple reaches a minimum at $\theta_e = 30°$ and a maximum at $\theta_e = 210°$. For all six sequences, the current ripple reaches its minimum at intervals of 60° during the electrical cycle.

Figs. 11 and 12 show the dq-axis instantaneous current ripples of sequences $(V_1V_6V_2V_5V_4V_3)$ and $(V_4V_3V_2V_5V_1V_6)$ at $\theta_e = 30°$, which correspond to the minimum and maximum of the total current ripple, respectively. The magnitude of each current ripple is zero at both the start and the end of the modulation period. The difference between the two instantaneous current ripples can be observed visually under dq-axis since the sequence $(V_4V_3V_2V_5V_1V_6)$ produces a large d-axis current ripple.

Fig. 13 shows the total current ripple I^2_{ripple} generated by all the six MSVPWM schemes, with respect to the angle of the average output voltage vector $\boldsymbol{e}$ when e_m is set to 0.2 of $\sqrt{2/3}V_{\text{dc}}$. It should be noted that e_{m} does not influence the corresponding

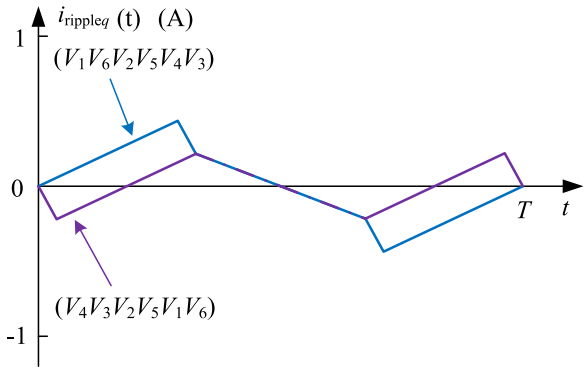

Fig. 12. q-axis instantaneous current ripple of sequences $(V_1V_6V_2V_5V_4V_3)$ and $(V_4V_3V_2V_5V_1V_6)$ at $\theta_e = 30°$.

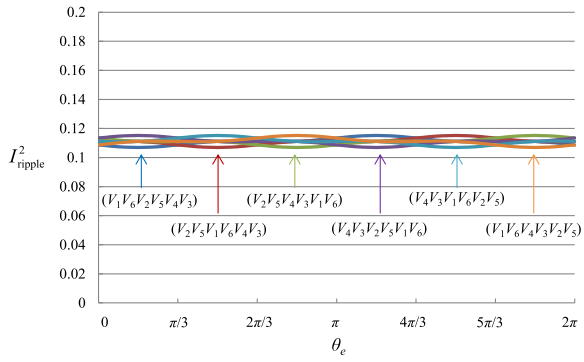

Fig. 13. Relation of the current ripple to the angle of the average output voltage vector when e_m is 0.2 of $\sqrt{2/3}V_{\text{dc}}$.

TABLE I
PROPOSED MSVPWM SCHEMES FOR LOW SALIENCY RATIO WHEN $\Delta\theta_e = 0$

θ_e	MSVPWM Sequences
[0° – 60°]	$(V_1V_6V_2V_5V_4V_3)$
[60° – 120°]	$(V_2V_5V_1V_6V_4V_3)$
[120° – 180°]	$(V_2V_5V_4V_3V_1V_6)$
[180° – 240°]	$(V_4V_3V_2V_5V_1V_6)$
[240° – 300°]	$(V_4V_3V_1V_6V_2V_5)$
[300° – 360°]	$(V_1V_6V_4V_3V_2V_5)$

angles of the extrema. However, a small e_m corresponds to a smaller difference between current ripple extrema, lowers the average current ripple.

According to Fig. 10, the MSVPWM scheme can be designed to change depending on the interval of 60°, as shown in Table I. Fig. 14 shows the current ripple I^2_{ripple} in its average under the conventional MSVPWM, and average under the proposed MSVPWM during electrical cycle, respectively. The current ripple I^2_{ripple}, which means harmonic copper loss, can be reduced about 23% at most with the proposed MSVPWM schemes. Furthermore, I^2_{ripple} is 0.099 at $e_m = 0$. That means MSVPWM provides sufficient harmonic excitation even at zero-speed operation. Because a small e_m results in a reduced range ability of current ripple during electrical cycle, the proposed MSVPWM works signally when the average output voltage vector $\boldsymbol{e}$ is large.

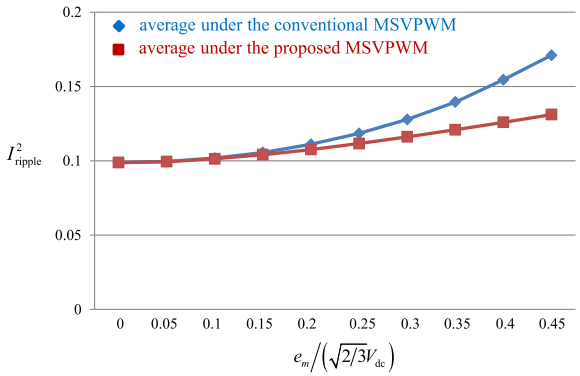

Fig. 14. Proper of the current ripple with respect to the magnitude of the average output voltage vector.

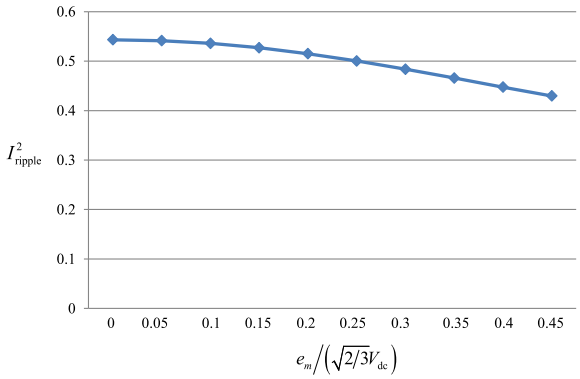

Fig. 15. Proper of the current ripple with respect to the magnitude of the average output voltage vector under the counterclockwise sequence $(V_1V_3V_2V_6V_4V_5)$.

As a comparison, Fig. 15 shows the current ripple I^2_{ripple} under the counterclockwise sequence $(V_1V_3V_2V_6V_4V_5)$ during electrical cycle. In this sequence, the switching times is 1/2 of the proposed MSVPWM, however, the current ripple I^2_{ripple} is as about four times as that of the proposed MSVPWM, which means the current ripple I^2_{ripple} per unit switching time is as two times as that of the proposed MSVPWM.

C. Influence of High Saliency Ratio

Since the *dq*-axis inductances essentially determine the current ripple corresponding to any error voltage, the magnetic saliency ratio affects the characteristics of the current ripple. The corresponding θ_e of the minimum and maximum current ripple is changed.

Figs. 16 and 17 show the total current ripple of the six available MSVPWM schemes with respect to the angle of the average output voltage vector $\boldsymbol{e}$ when e_m is set to 0.4 of $\sqrt{2/3}V_{\text{dc}}$, $L_q = 25$ mH, $L_d = 16.67$ and 12.5 mH, respectively. It is found that when the saliency ratio is increased, the current ripple reaches its minimum at intervals of 30° during the electrical cycle, because the high saliency ratio makes the *d*-axis component of the current ripple serious. Moreover, the high saliency ratio does not cause horizontal shift in current ripple characteristics. In this case, the MSVPWM scheme can be designed to change depending on the interval of 30°, as shown in Table II.

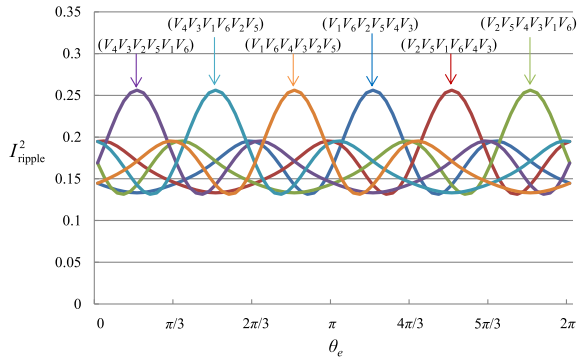

Fig. 16. Relation of the total current ripple to the angle of the average output voltage vector when e_m is 0.4 of $\sqrt{2/3}V_{\text{dc}}$, $L_d = 16.67$ mH, $L_q = 25$ mH.

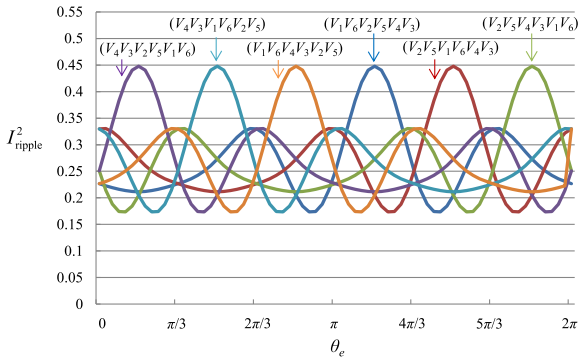

Fig. 17. Relation of the total current ripple to the angle of the average output voltage vector when e_m is 0.4 of $\sqrt{2/3}V_{\text{dc}}$, $L_d = 12.5$ mH, and $L_q = 25$ mH.

TABLE II
PROPOSED MSVPWM SCHEMES FOR HIGH SALIENCY RATIO WHEN $\Delta\theta_e = 0$

θ_e	MSVPWM Sequences	θ_e	MSVPWM Sequences
$[0° - 30°]$	$(V_2V_5V_4V_3V_1V_6)$	$[180° - 210°]$	$(V_1V_6V_4V_3V_2V_5)$
$[30° - 60°]$	$(V_4V_3V_1V_6V_2V_5)$	$[210° - 240°]$	$(V_2V_5V_1V_6V_4V_3)$
$[60° - 90°]$	$(V_4V_3V_2V_5V_1V_6)$	$[240° - 270°]$	$(V_1V_6V_2V_5V_4V_3)$
$[90° - 120°]$	$(V_1V_6V_4V_3V_2V_5)$	$[270° - 300°]$	$(V_2V_5V_4V_3V_1V_6)$
$[120° - 150°]$	$(V_4V_3V_1V_6V_2V_5)$	$[300° - 330°]$	$(V_2V_5V_1V_6V_4V_3)$
$[150° - 180°]$	$(V_1V_6V_2V_5V_4V_3)$	$[330° - 360°]$	$(V_4V_3V_2V_5V_1V_6)$

TABLE III
SUMMARY OF SWITCH SELECTOR s_k

Sector	Phase of $\boldsymbol{e}$	Active s_k	Inactive s_k
I	$[-30°\sim 30°]$	$s_{0,1,3,5}$	$s_{2,4,6,7}$
II	$[30°\sim 90°]$	$s_{1,2,3,7}$	$s_{0,4,5,6}$
III	$[90°\sim 150°]$	$s_{0,2,3,6}$	$s_{1,4,5,7}$
IV	$[150°\sim 210°]$	$s_{2,4,6,7}$	$s_{0,1,3,5}$
V	$[210°\sim 270°]$	$s_{0,4,5,6}$	$s_{1,2,3,7}$
VI	$[270°\sim 330°]$	$s_{1,4,5,7}$	$s_{0,2,3,6}$

According to Fig. 16, the critical saliency ratio between these two types of MSVPWM is 1.5 approximately.

D. Mirrored Sequences

Note that the fixed switching sequences (V_6V_1), (V_5V_2), (V_3V_4) can also reduce the three-phase current ripple. Keeping

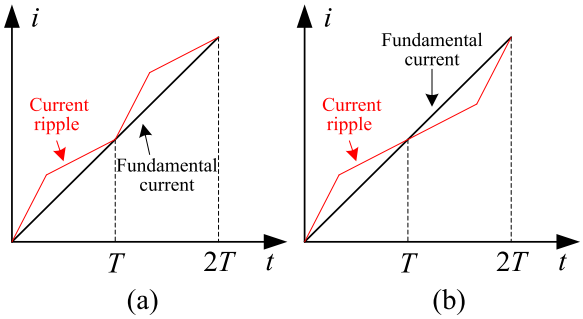

Fig. 18. Sketch of the fundamental current and the current ripple during two modulation period. (a) Proposed schemes. (b) Alternant schemes with mirrored sequence.

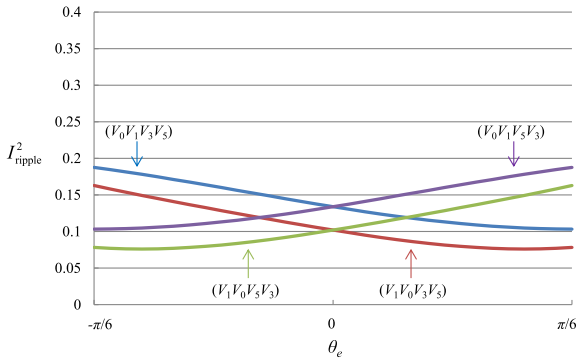

Fig. 19. Relation of the total current ripple to the angle of the average output voltage vector under four voltage vectors MSVPWM when e_m is 0.35 of $\sqrt{2/3}V_{\text{dc}}$, $L_d = 20$ mH, and $L_q = 20$ mH.

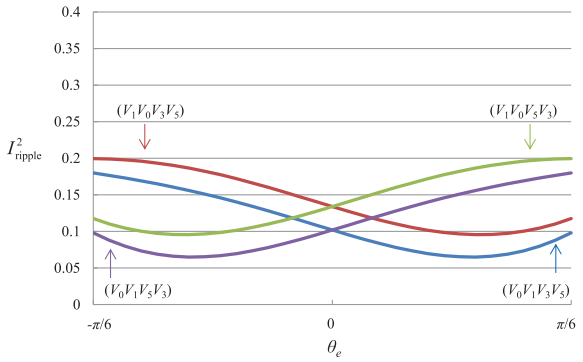

Fig. 20. Relation of the total current ripple to the angle of the average output voltage vector under four voltage vectors MSVPWM when e_m is 0.65 of $\sqrt{2/3}V_{\text{dc}}$, $L_d = 20$ mH, and $L_q = 20$ mH.

three-phase symmetry, the MSVPWM schemes made from the aforementioned fixed switching sequences have mirror symmetry to the basic sequences. For example, $(V_3V_4V_5V_2V_6V_1)$ is the mirrored sequence of the basic sequence $(V_1V_6V_2V_5V_4V_3)$.

The similarity between them is the corresponding sequence product the same RMS of current ripple. The difference is the opposite polarity of average current ripple during a modulation period. The switching sequence that alternately employs the basic sequences and mirrored sequences in every modulation period maintains the reduced RMS current ripple while average current ripples is mutually offsetting during every two modulation periods, as shown in Fig. 18. Since the cumulative error

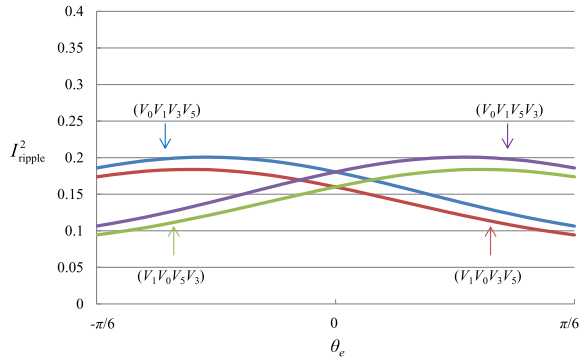

Fig. 21. Relation of the total current ripple to the angle of the average output voltage vector under four voltage vectors MSVPWM when e_m is 0.35 of $\sqrt{2/3}V_{\text{dc}}$, $L_d = 12.5$ mH, and $L_q = 25$ mH.

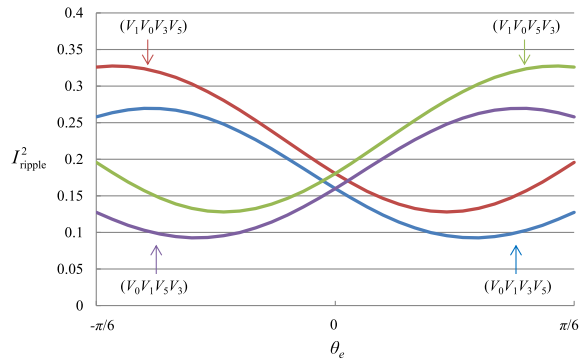

Fig. 22. Relation of the total current ripple to the angle of the average output voltage vector under four voltage vectors MSVPWM when e_m is 0.65 of $\sqrt{2/3}V_{\text{dc}}$, $L_d = 12.5$ mH, $L_q = 25$ mH.

of average current is reduced near-zero, this hybrid sequences are conducive to closed-loop current control, however, the HF components of $1/2T$ Hz and its integral multiples of frequency are emerged then lead to a deteriorated acoustic noise. For this reason, the hybrid schemes with mirrored sequences are not introduced.

E. MSVPWM for High-Speed Operation

To ensure the range of the average output voltage vector as large as possible, the closest three nonzero voltage vectors of the average output voltage vector $\boldsymbol{e}$ and one zero voltage vector, in other words, four voltage vectors are selected for an MSVPWM scheme for high-speed operation. Table III shows the relationship between the phase of $\boldsymbol{e}$ and the value of switch selector s_k [24].

Take sector I for example, in this case, (14) can be expressed legibly as

$$\begin{bmatrix} \zeta_0 & \zeta_4 \\ \zeta_1 & \zeta_5 \\ \zeta_2 & \zeta_6 \\ \zeta_3 & \zeta_7 \end{bmatrix} = \begin{bmatrix} -\dfrac{\sqrt{6}e_\alpha}{2V_{\text{dc}}} + \dfrac{3}{4} & 0 \\ \dfrac{\sqrt{6}e_\alpha}{2V_{\text{dc}}} - \dfrac{1}{4} & -\dfrac{\sqrt{2}e_\beta}{2V_{\text{dc}}} + \dfrac{1}{4} \\ 0 & 0 \\ \dfrac{\sqrt{2}e_\beta}{2V_{\text{dc}}} + \dfrac{1}{4} & 0 \end{bmatrix}. \tag{25}$$

TABLE IV
CONVENTIONAL MSVPWM SCHEME FOR HIGH-SPEED OPERATION

θ_e	MSVPWM Sequences
$[-30° - 30°]$	$(V_0 V_1 V_3 V_5)$
$[30° - 90°]$	$(V_7 V_3 V_2 V_1)$
$[90° - 150°]$	$(V_0 V_2 V_6 V_3)$
$[150° - 210°]$	$(V_7 V_6 V_4 V_2)$
$[210° - 270°]$	$(V_0 V_4 V_5 V_6)$
$[270° - 330°]$	$(V_7 V_5 V_1 V_4)$

TABLE V
PROPOSED MSVPWM SCHEME FOR HIGH-SPEED OPERATION WHEN $\Delta\theta_e = 0$

θ_e	$e_m < 0.5(\sqrt{2/3}V_{\rm dc})$	$e_m > 0.5(\sqrt{2/3}V_{\rm dc})$
$[0° - 30°]$	$(V_1 V_0 V_3 V_5)$	$(V_0 V_1 V_3 V_5)$
$[30° - 60°]$	$(V_3 V_7 V_1 V_2)$	$(V_7 V_3 V_1 V_2)$
$[60° - 90°]$	$(V_3 V_7 V_2 V_1)$	$(V_7 V_3 V_2 V_1)$
$[90° - 120°]$	$(V_2 V_0 V_3 V_6)$	$(V_0 V_2 V_3 V_6)$
$[120° - 150°]$	$(V_2 V_0 V_6 V_3)$	$(V_0 V_2 V_6 V_3)$
$[150° - 180°]$	$(V_6 V_7 V_2 V_4)$	$(V_7 V_6 V_2 V_4)$
$[180° - 210°]$	$(V_6 V_7 V_4 V_2)$	$(V_7 V_6 V_4 V_2)$
$[210° - 240°]$	$(V_4 V_0 V_6 V_5)$	$(V_0 V_4 V_6 V_5)$
$[240° - 270°]$	$(V_4 V_0 V_5 V_6)$	$(V_0 V_4 V_5 V_6)$
$[270° - 300°]$	$(V_5 V_7 V_4 V_1)$	$(V_7 V_5 V_4 V_1)$
$[300° - 330°]$	$(V_5 V_7 V_1 V_4)$	$(V_7 V_5 V_1 V_4)$
$[330° - 360°]$	$(V_1 V_0 V_5 V_3)$	$(V_0 V_1 V_5 V_3)$

In the other sectors, ζ_k has a similar expression as (25) because of the symmetrical characteristic of sectors and output voltage vectors. With the limit of $0 < \zeta_k < 1$, the value of e_m /$(\sqrt{2/3}V_{\rm dc})$ must be more than 28.87% and the maximum is the same as sine–triangle PWM for a sinusoidal output.

Similar to the MSVPWM with six voltage vectors, $(V_0 V_1)$, $(V_3 V_5)$, $(V_1 V_0)$, and $(V_5 V_3)$ are combined as fixed switching sequences to reduce the current ripple. Eliminate the mirrored sequences, there are four valid schemes $[(V_0 V_1 V_3 V_5)$, $(V_1 V_0 V_3 V_5)$, $(V_1 V_0 V_5 V_3)$ and $(V_0 V_1 V_5 V_3)]$. Here, zero voltage vectors V_0 and V_7 are selected flexibly to balance the switching events of each phase during a modulation period for different sectors.

Figs. 19–22 show the relation of the total current ripple to the angle of the average output voltage vector under four voltage vectors MSVPWM schemes with different e_m and saliency ratio. The four voltage vectors MSVPWM scheme for reducing current ripple can be determined by the magnitude and the phase of the average output voltage vector, which the critical value are $0.5(\sqrt{2/3}V_{\rm dc})$ and 0°, respectively. In this case, the influence of saliency ratio to the selection of optimized MSVPWM schemes seems slight because most error voltage vectors are generated in d-axis. Table IV gives the conventional four-vector MSVPWM sequences of all six sectors. Table V gives proposed four-vector MSVPWM sequences of all six sectors, the average current ripple can reach minimum every 30°.

Fig. 23 shows the current ripple $I^2_{\rm ripple}$ in its average under the conventional MSVPWM for high-speed operation, and average under the proposed MSVPWM for high-speed operation during electrical cycle, respectively. Here, $L_d = 20$ mH, $L_q = 20$ mH. The harmonic copper loss can be reduced about 40% at most.

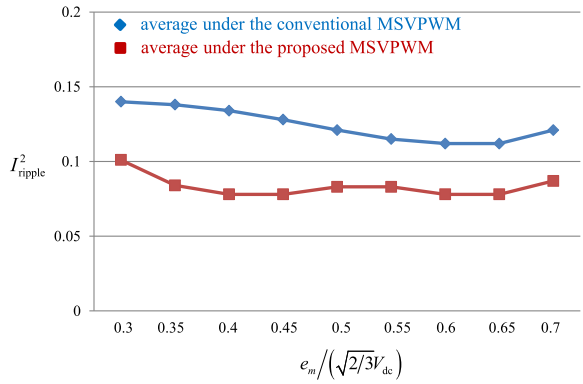

Fig. 23. Proper of the current ripple with respect to the magnitude of the average output voltage vector for high-speed operation.

TABLE VI
IPMSM PARAMETERS

Rated power	1.5 kW
Rated speed	1150 r/min
Rated current	5.7 A
Rated voltage	187 V
Phase resistance	1.071 Ω
PM flux linkage	0.45 Wb
Pole pairs	3
L_q (estimated)	23.7 mH at 0 A
L_d (estimated)	12.0 mH at 0 A
Saliency Ratio	1.98

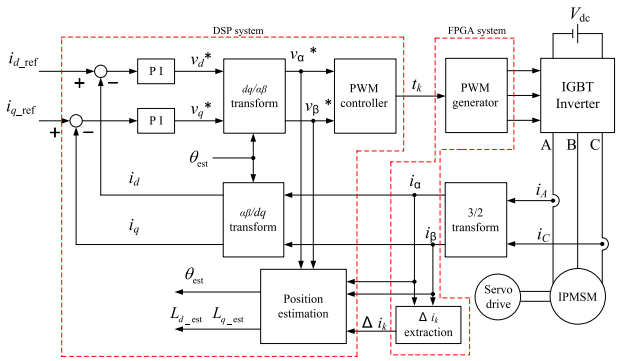

Fig. 24. Block diagram of the proposed sensorless control system.

F. *Influence of* $\Delta\theta_e$

A shift angle of proposed interval occurs when $\Delta\theta_e$ is nonzero. The simplified variations based on curve fitting with $\Delta\theta_e$, which is assumed in 0°–90° are described as follows:

1) for Table I, no shift occurs;
2) for Table II, the characteristics of current ripple shift to the right with increased $\Delta\theta_e$, and the shift angle $\theta_{\rm shift}$ can be calculated approximately by

$$\theta_{\rm shift} \approx 0.50 \times \Delta\theta_e. \tag{26}$$

3) for Table V, $\theta_{\rm shift}$ depends on both e_m and $\Delta\theta_e$, and $\theta_{\rm shift}$ can be calculated approximately by the following equations:

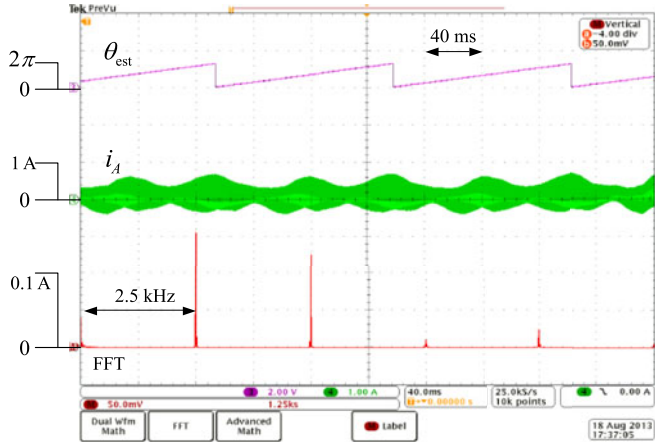

Fig. 25. FFT spectrum of the line current under the conventional MSVPWM at 160 r/min and no load. From top: estimated position angle, line current and FFT spectrum.

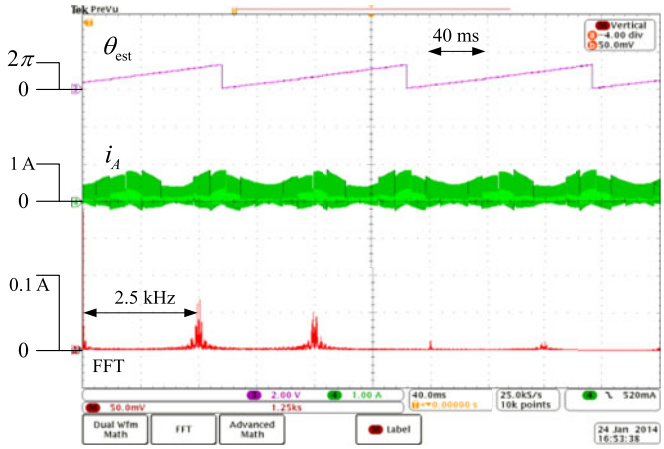

Fig. 27. FFT spectrum of the line current under the proposed MSVPWM for high saliency ratio at 160 r/min and no load. From top: Estimated position angle, line current, and FFT spectrum.

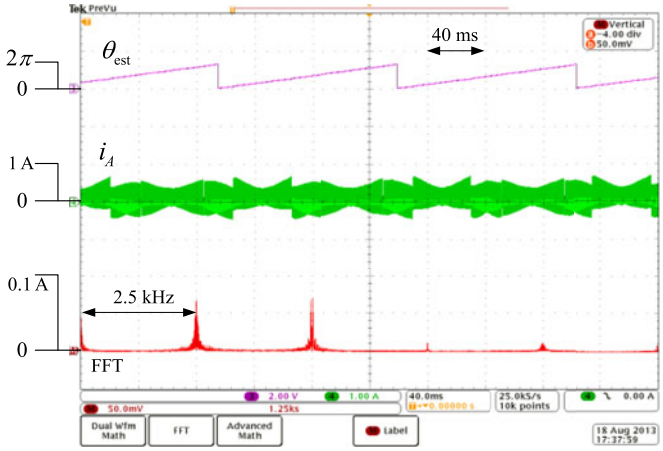

Fig. 26. FFT spectrum of the line current under the proposed MSVPWM for low saliency ratio at 160 r/min and no load. From top: Estimated position angle, line current, and FFT spectrum.

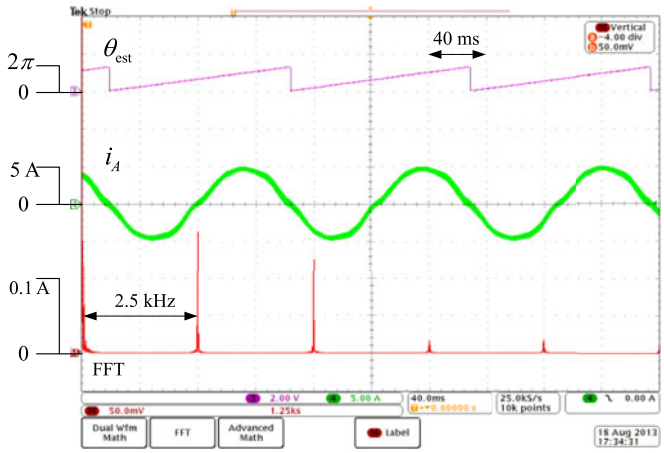

Fig. 28. FFT spectrum of the line current under the conventional MSVPWM at 160 r/min and rated load. From top: Estimated position angle, line current, and FFT spectrum.

$$\mathrm{A_{max}} \approx -177.78 \times \left(\frac{\mathrm{e}_m}{\sqrt{2/3}\mathrm{V_{dc}}}\right)^2 + 244.44 \times \left(\frac{\mathrm{e}_m}{\sqrt{2/3}\mathrm{V_{dc}}}\right) - 77.78 \quad (27)$$

$$\theta_{\mathrm{shift}} \approx \mathrm{A_{max}} \times \sin(2\Delta\theta_e). \quad (28)$$

In the experiential results, since the actual range of $\Delta\theta_e$ is about 0°–11°, the maximum of θ_{shift} is within only 4°.

VI. Experimental Results

A. System Configuration

The effectiveness of the proposed MSVPWM schemes is tested experimentally. A block diagram of the sensorless drive system is shown in Fig. 24. The MSVPWM signals are generated on an XC2S200 field-programmable gate array (FPGA) board. A C6713 digital signal processor card is used to carry out the following real-time algorithm: closed-loop current control, position estimation, and inductance estimation. A three-phase insulated-gate bipolar transistor intelligent power module is used as an inverter. In the experiments, the modulation period of the drive is set to 400 μs, and the dead time is set to 3.9 μs. The motor parameters are shown in Table VI.

The authors' previous report [26] discussed in detail how inverter nonlinear effects such as dead-time affect the performance of methods based on MSVPWM. In brief, the influence of the inverter nonlinear effects on this sensorless drive system seems minor.

B. Harmonic Components of Phase Current

Figs. 25–27 show the line currents and corresponding fast fourier transform (FFT) spectra of the conventional MSVPWM, the proposed MSVPWM for low saliency ratio and the proposed MSVPWM for high saliency ratio, respectively. The *dq*-axis reference currents i_{d_ref} and i_{q_ref} are set to zero. A servo drive system connected to the shaft of the IPMSM controls the speed so it remains at a constant 160 r/min. In the conventional MSVPWM, harmonic components are observed around frequencies, which

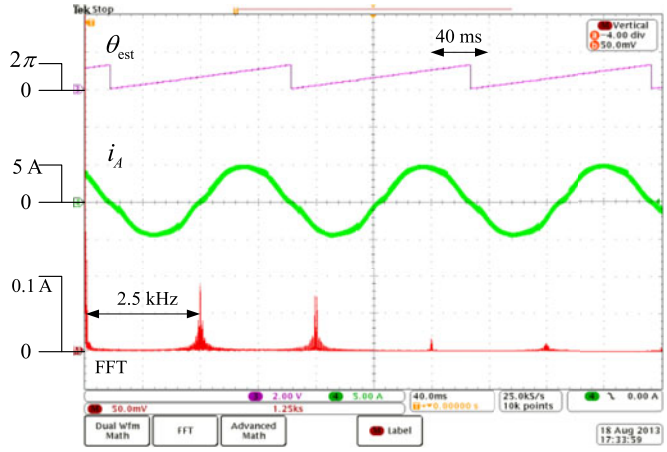

Fig. 29. FFT spectrum of the line current under the proposed MSVPWM for low saliency ratio at 160 r/min and rated load. From top: Estimated position angle, line current, and FFT spectrum.

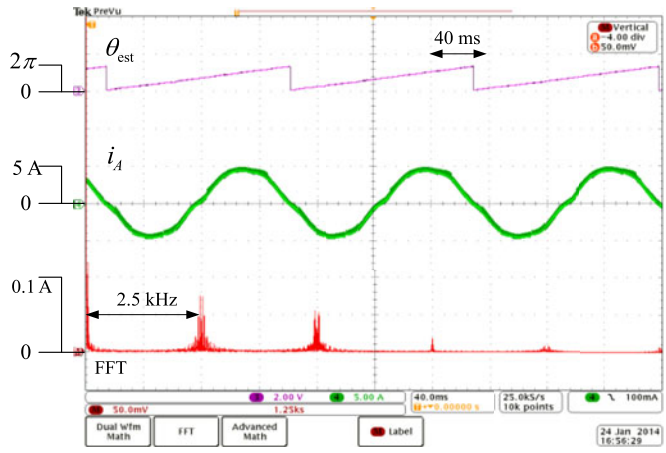

Fig. 30. FFT spectrum of the line current under the proposed MSVPWM for high saliency ratio at 160 r/min and rated load. From top: estimated position angle, line current, and FFT spectrum.

are integer multiples of the modulation frequency. In contrast, with both of the proposed MSVPWM schemes for low/high saliency ratio, the spectra are more decentralized, and the 2.5, 5, and 10 kHz components are significantly reduced. Furthermore, since the estimated saliency ratio in Table VI is about 1.98, which is larger than the critical saliency ratio of 1.5 in Section IV-C, the proposed MSVPWM scheme for high saliency ratio is more effective to reduce current ripple than the scheme for low saliency ratio, as comparing Fig. 27 with Fig. 26.

Figs. 28–30 show the line currents and corresponding FFT spectra of the conventional, the proposed MSVPWM scheme for low saliency ratio and the proposed MSVPWM scheme for high saliency ratio at 160 r/min, respectively. The d-axis reference current i_{d_ref} is set to zero, and the q-axis reference current i_{q_ref} is set to 5.7 A. The improvement in terms of harmonic components is similar to that seen in Figs. 25–27.

For an unknown-parameter IPMSM, the selection of the proposed MSVPWM scheme for low or high saliency ratio can be determined by the online dq-axis inductance estimation [33], as discussed in Section VI-D.

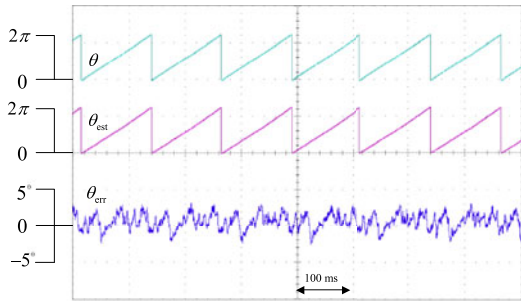

Fig. 31. Measured signals in sensorless control under the conventional MSVPWM at 160 r/min and $i_q = 0$. From top: true position angle, estimated position angle, and estimation error.

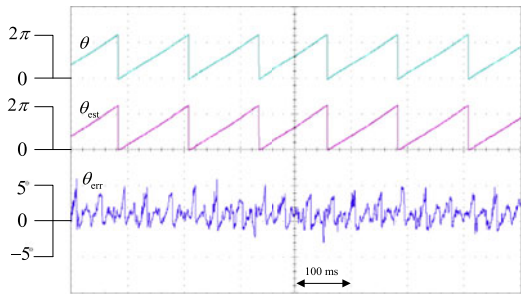

Fig. 32. Measured signals in sensorless control under the proposed MSVPWM for low saliency ratio at 160 r/min and $i_q = 0$. From top: True position angle, estimated position angle, and estimation error.

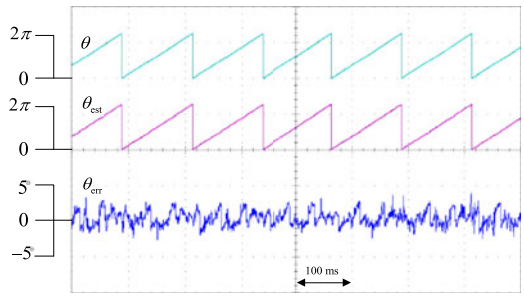

Fig. 33. Measured signals in sensorless control under the proposed MSVPWM for high saliency ratio at 160 r/min and $i_q = 0$. From top: True position angle, estimated position angle, and estimation error.

C. Position Estimation

Since the proposed MSVPWM schemes change the trajectory of the response current during a modulation period, the performance of rotor position estimation under the proposed MSVPWM schemes should be compared with that under the conventional scheme.

Figs. 31–33 show the characteristics of the position error θ_{err} between the actual position θ and the estimated position θ_{est} under the conventional MSVPWM, the proposed MSVPWM for low saliency ratio and the proposed MSVPWM for high saliency ratio at 160 r/min, respectively, while i_{d_ref} is set to zero and i_{q_ref} is set to zero. The actual position θ is measured by a pulse generator (1024 ppr) attached to the shaft of the IPMSM. The results suggest that the sensorless drive system based on MSVPWM provides accurate position estimation with fluctuation in the range of about $\pm 5°$, which is independent of the MSVPWM schemes.

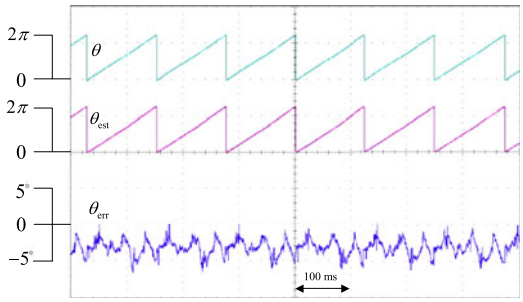

Fig. 34. Measured signals in sensorless control under the conventional MSVPWM at 160 r/min and $i_q = 5.7$ A. From top: True position angle, estimated position angle, and estimation error.

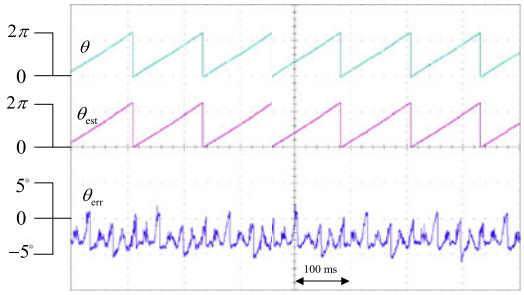

Fig. 35. Measured signals in sensorless control under the proposed MSVPWM for low saliency ratio at 160 r/min and $i_q = 5.7$ A. From top: True position angle, estimated position angle, and estimation error.

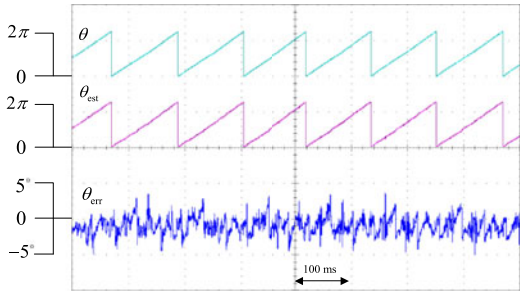

Fig. 36. Measured signals in sensorless control under the proposed MSVPWM for high saliency ratio at 160 r/min and $i_q = 5.7$ A. From top: True position angle, estimated position angle, and estimation error.

Figs. 34–36 show the characteristics of the position error $\theta_{\rm err}$ between the actual position θ and the estimated position $\theta_{\rm est}$ under the conventional MSVPWM and the proposed hybrid MSVPWM at 160 r/min, respectively, while $i_{d\_\rm ref}$ is set to zero and $i_{q\_\rm ref}$ is set to 5.7 A. It means that the sensorless drive systems based on any MSVPWM schemes provide accurate estimated rotor position even under magnetic saturation produced by the increased stator current.

D. Inductance Estimation

The rotor position is obtained by estimating the phase inductances. Consequently, not only the rotor position but also the inductance parameter values can be estimated instantaneously during a period of modulation with MSVPWM scheme [33].

Figs. 37–39 show the inductance estimation of the conventional MSVPWM, the proposed MSVPWM for low saliency ratio and the proposed MSVPWM for high saliency ratio at 160 r/min, respectively, while $i_{d\_\rm ref}$ and $i_{q\_\rm ref}$ are set to zero.

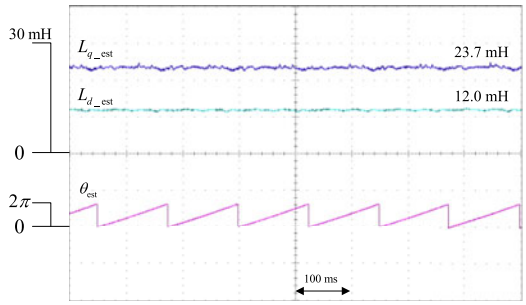

Fig. 37. Measured signals in sensorless control under the conventional MSVPWM at 160 r/min and $i_q = 0$. From top: Estimated q-axis inductance, estimated d-axis inductance, and estimated position angle.

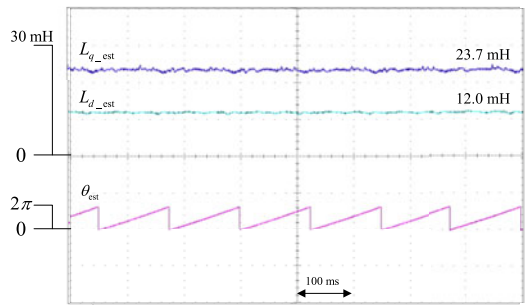

Fig. 38. Measured signals in sensorless control under the proposed MSVPWM for low saliency ratio at 160 r/min and $i_q = 0$. From top: Estimated q-axis inductance, estimated d-axis inductance, and estimated position angle.

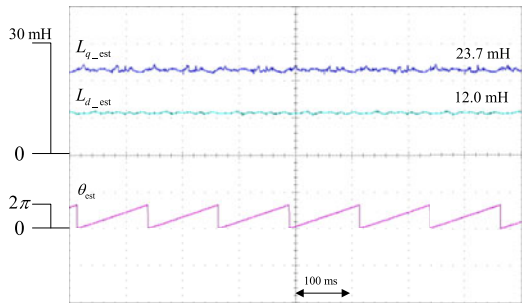

Fig. 39. Measured signals in sensorless control under the proposed MSVPWM for high saliency ratio at 160 r/min and $i_q = 0$. From top: Estimated q-axis inductance, estimated d-axis inductance, and estimated position angle.

Figs. 40–42 show the inductance estimation of the conventional and the proposed MSVPWM schemes at 160 r/min, respectively, while $i_{d\_\rm ref}$ is set to zero and $i_{q\_\rm ref}$ is set to 5.7 A. The average estimated q-axis inductance $L_{q\_\rm est}$ is reduced by about 11.8%, from 23.7 to 20.9 mH, with respect to $i_{q\_\rm ref}$, which ranges from 0 to the rated current because the saturation becomes fuller as current builds up in the q-axis.

The results show that the proposed schemes have no influence on inductance estimation. Therefore, for an unknown-parameter IPMSM, the most effective MSVPWM can be determined by the any of the MSVPWM schemes. The estimated d-axis inductance is an essential parameter for magnet polarity identification. The required minimum d-axis current for the magnet polarity identification is small because of the accuracy and stability of the estimated inductances [27].

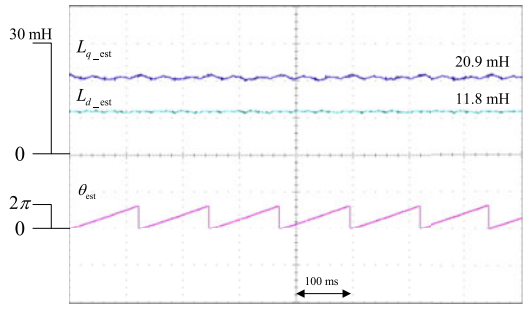

Fig. 40. Measured signals in sensorless control under the conventional MSVPWM at 160 r/min and $i_q = 5.7$ A. From top: Estimated q-axis inductance, estimated d-axis inductance, and estimated position angle.

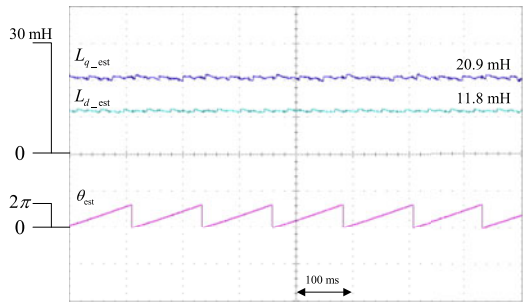

Fig. 41. Measured signals in sensorless control under the proposed MSVPWM for low saliency ratio at 160 r/min and $i_q = 5.7$ A. From top: Estimated q-axis inductance, estimated d-axis inductance, and estimated position angle.

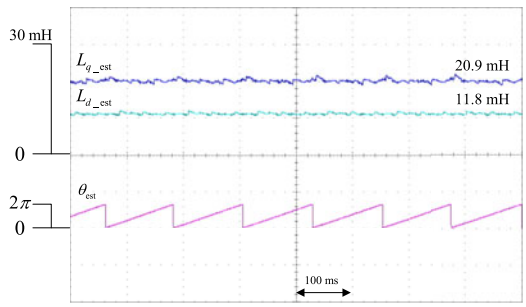

Fig. 42. Measured signals in sensorless control under the proposed MSVPWM for high saliency ratio at 160 r/min and $i_q = 5.7$ A. From top: Estimated q-axis inductance, estimated d-axis inductance, and estimated position angle.

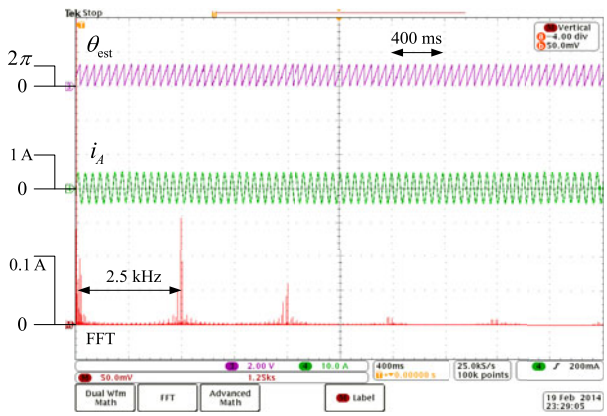

Fig. 43. FFT spectrum of the line current under the conventional MSVPWM for high speed at 360 r/min and $i_q = 5.7$ A. From top: Estimated position angle, line current, and FFT spectrum.

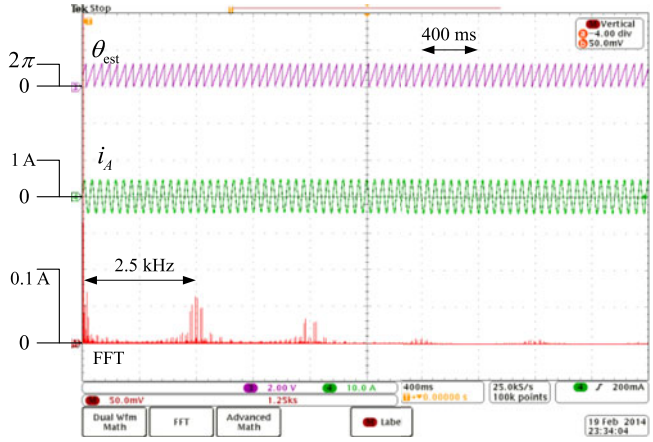

Fig. 44. FFT spectrum of the line current under the proposed MSVPWM for high speed at 360 r/min and $i_q = 5.7$ A. From top: Estimated position angle, line current, and FFT spectrum.

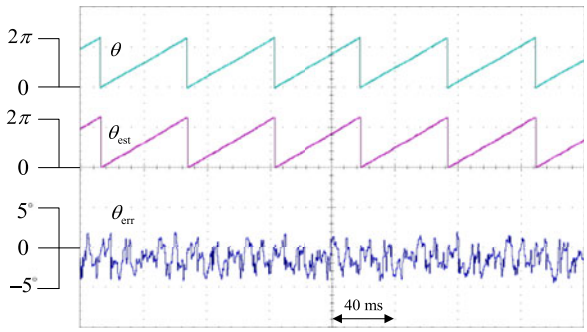

Fig. 45. Measured signals in sensorless control under the conventional MSVPWM for high speed at 360 r/min and $i_q = 5.7$ A. From top: true position angle, estimated position angle, and estimation error.

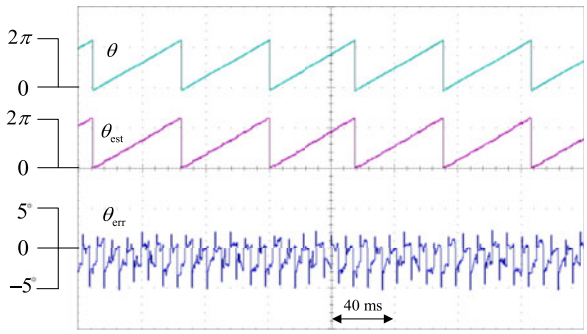

Fig. 46. Measured signals in sensorless control under the proposed MSVPWM for high speed at 360 r/min and $i_q = 5.7$ A. From top: True position angle, estimated position angle, and estimation error.

E. MSVPWM for High-Speed Operation

Figs. 43 and 44 show the line currents and corresponding FFT spectra of the conventional and proposed MSVPWM for high-speed operation, respectively. i_{d_ref} is set to zero, i_{q_ref} is set to 5.7 A. The speed remains at a constant 360 r/min (18 Hz). The improvement in terms of harmonic components is similar to that seen in MSVPWM for low-speed operation.

Figs. 45 and 46 show the position estimation of the conventional and proposed MSVPWM for high-speed operation, respectively. Figs. 47 and 48 show the inductance estimation of

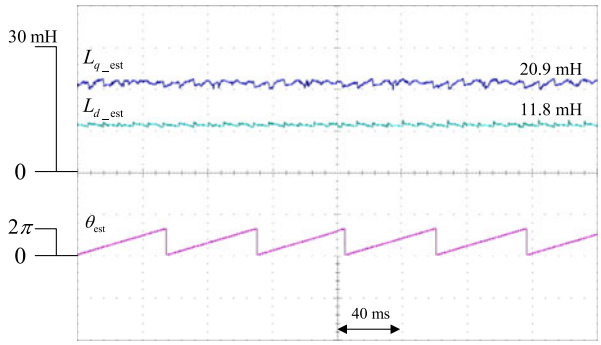

Fig. 47. Measured signals in sensorless control under the conventional MSVPWM for high speed at 360 r/min and $i_q = 5.7$ A. From top: Estimated q-axis inductance, estimated d-axis inductance, and estimated position angle.

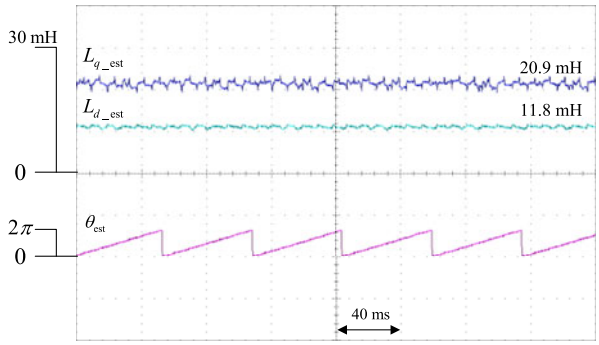

Fig. 48. Measured signals in sensorless control under the proposed MSVPWM for high speed at 360 r/min and $i_q = 5.7$ A. From top: estimated q-axis inductance, estimated d-axis inductance, and estimated position angle.

the conventional and proposed MSVPWM for high-speed operation, respectively. The results show that the proposed MSVPWM for high-speed operation have almost no influence on position estimation and inductance estimation as well.

VII. Conclusion

Position estimation cannot work perfectly in standard SVPWM for zero- and low-speed operation of the IPMSM. To eliminate this drawback of SVPWM and increase the efficiency of the HF effect at arbitrary the average output voltage vector $\boldsymbol{e}$, MSVPWM is adopted. In this paper, hybrid MSVPWM schemes are proposed for low/high saliency ratio where the switching sequence is designed to change depending on the angle range. Since the sequences of the dq-axis error voltage vectors are adjusted to bring the dq-axis current ripple closer to zero during a modulation period, consequently, the average current ripple can reach minimum every $60^\circ/30^\circ$. Theoretically, the average current ripple can be reduced by about 10% with the proposed method. Experimental results at low-speed, $i_d = 0$ operation confirm that the proposed MSVPWM schemes lead to a significant reduction in harmonic current while maintaining high performance of sensorless estimation. The proposed method can be implemented without increasing any hardware cost.

Appendix

(1) is expressed concisely as follows:

$$\boldsymbol{E} = \boldsymbol{F}\boldsymbol{Z}. \tag{A1}$$

Here, $\boldsymbol{E}$ is $[e_\alpha e_\beta 1]^T$, $\boldsymbol{Z}$ is $[\zeta_0 \zeta_1 \ldots \zeta_7]^T$, and $\boldsymbol{F}$ is the voltage vector matrix.

The objective functional is defined as follows:

$$\boldsymbol{J} = \boldsymbol{Z}^T \boldsymbol{Z}. \tag{A2}$$

The Lagrange equation can be defined as follows:

$$\boldsymbol{L} = \boldsymbol{Z}^T \boldsymbol{Z} - \boldsymbol{\lambda}^T (\boldsymbol{F}\boldsymbol{Z} - \boldsymbol{E}) \tag{A3}$$

where λ is the Lagrange multiplier. The partial derivatives of $\boldsymbol{L}$ with respect to $\boldsymbol{Z}$ and λ are shown as follows:

$$\frac{\partial \boldsymbol{L}}{\partial \boldsymbol{Z}} = 2\boldsymbol{Z} - \boldsymbol{F}^T \boldsymbol{\lambda} = 0 \tag{A4}$$

$$\frac{\partial \boldsymbol{L}}{\partial \boldsymbol{\lambda}} = \boldsymbol{F}\boldsymbol{Z} - \boldsymbol{E} = 0. \tag{A5}$$

If $\boldsymbol{F}\boldsymbol{F}^T$ has full row rank, the Lagrange multiplier can be deduced from (A4) and (A5) as

$$\boldsymbol{\lambda} = 2(\mathbf{F}\mathbf{F}^T)^{-1}\boldsymbol{E}. \tag{A6}$$

$\boldsymbol{Z}$ can be expressed as follows:

$$\boldsymbol{Z} = \boldsymbol{F}^T (\mathbf{F}\mathbf{F}^T)^{-1}\boldsymbol{E}. \tag{A7}$$

The right pseudoinverse matrix is defined from the aforementioned equation as

$$\boldsymbol{F}^{\mathrm{RM}} = \boldsymbol{F}^T (\mathbf{F}\mathbf{F}^T)^{-1}. \tag{A8}$$

The least-squares solution for the sum of ζ_k can be calculated with the help of (A8).

References

[1] S. Morimoto, "Trend of permanent magnet synchronous machines," *IEEJ Trans. Elect. Electron. Eng.*, vol. 2, no. 2, pp. 101–108, Feb. 2007.
[2] T. Noguchi, "Trends of permanent-magnet synchronous machine drives," *IEEJ Trans. Elect. Electron. Eng.*, vol. 2, no. 2, pp. 125–142, Feb. 2007.
[3] W. Shi and Z. Zhang, "Multiobjective optimum design method with anti-demagnetization of high-density permanent magnet synchronous motor," *IEEJ Trans. Elect. Electron. Eng.*, vol. 9, no. 5, pp. 555–562, Sep. 2014.
[4] A. Imura, T. Takahashi, M. Fujisuna, T. Zanma, and S. Doki, "Improved PMSM model considering flux characteristics for model predictive-based current control," *IEEJ Trans. Elect. Electron. Eng.*, vol. 10, no. 1, pp. 92–100, Jan. 2015.
[5] M. Seilmeier and B. Piepenbreier, "Sensorless control of PMSM for the whole speed range using two-degree-of-freedom current control and HF test current injection for low-speed range," *IEEE Trans. Power Electron.*, vol. 30, no. 8, pp. 4394–4403, Aug. 2015.
[6] M. Hasegawa and K. Matsui, "IPMSM position sensorless control based on adaptive flux observer using ε1-modification approach," *IEEJ Trans. Elect. Electron. Eng.*, vol. 4, no. 3, pp. 450–452, Apr. 2009.
[7] D. Paulus, J. F. Stumper, and R. Kennel, "Sensorless control of synchronous machines based on direct speed and position estimation in polar stator-current coordinates," *IEEE Trans. Power Electron.*, vol. 28, no. 5, pp. 2503–2513, May. 2013.
[8] S. Po-ngam and S. Sangwongwanich, "Stability and dynamic performance improvement of adaptive full-order observers for sensorless PMSM drive," *IEEE Trans. Power Electron.*, vol. 27, no. 2, pp. 588–600, Feb. 2012.
[9] Z. Wang, K. Lu, and F. Blaabjerg, "A simple startup strategy based on current regulation for back-EMF-based sensorless control of PMSM," *IEEE Trans. Power Electron.*, vol. 27, no. 8, pp. 3817–3825, Aug. 2012.
[10] Y. Zhao, W. Qiao, and L. Wu, "An adaptive quasi-sliding-mode rotor position observer-based sensorless control for interior permanent magnet synchronous machines," *IEEE Trans. Power Electron.*, vol. 28, no. 12, pp. 5618–5629, Dec. 2013.
[11] Y. Zhao, Z. Zhang, W. Qiao, and L. Wu, "An extended flux model-based rotor position estimator for sensorless control of salient-pole permanent-magnet synchronous machines," *IEEE Trans. Power Electron.*, vol. 30, no. 8, pp. 4412–4422, Aug. 2015.

[12] G. Wang, H. Zhan, and G. Zhang, "Adaptive compensation method of position estimation harmonic error for EMF-based observer in sensorless IPMSM drives," *IEEE Trans. Power Electron.*, vol. 29, no. 6, pp. 3055–3064, Jun. 2014.
[13] M. Boussak, "Implementation and experimental investigation of sensorless speed control with initial rotor position estimation for interior permanent magnet synchronous motor drive," *IEEE Trans. Power Electron.*, vol. 20, no. 6, pp. 1413–1422, Nov. 2005.
[14] J. Hu, J. Liu, and L. Xu, "Eddy current effects on rotor position estimation and magnetic pole identification of PMSM at zero and low speeds," *IEEE Trans. Power Electron.*, vol. 23, no. 5, pp. 2565–2575, Sep. 2008.
[15] M. Corley and R. D. Lorenz, "Rotor position and velocity estimation for a salient-pole permanent magnet synchronous machine at standstill and high speeds," *IEEE Trans. Ind. Appl.*, vol. 34, no. 4, pp. 784–789, Jul./Aug. 1998.
[16] J. Holtz, "Acquisition of position error and magnet polarity for sensorless control of PM synchronous machines," *IEEE Trans. Ind. Appl.*, vol. 44, no. 4, pp. 1172–1180, Jul./Aug. 2008.
[17] B. De, F. M. L,P. Sergeant, and J. A. Melkebeek, "A sensorless drive by applying test pulses without affecting the average-current Samples," *IEEE Trans. Power Electron.*, vol. 25, no. 4, pp. 875–888, Apr. 2010.
[18] M. A. M. Ghazi and F. Tahami, "Sensorless control of PMSMs with tolerance for delays and stator resistance uncertainties," *IEEE Trans. Power Electron.*, vol. 28, no. 3, pp .1391–1399, Mar. 2013.
[19] D. Raca, P. García, D. Reigosa, F. Briz, and R. D. Lorenz, "Carrier-signal selection for sensorless control of PM synchronous machines at zero and very low speeds," *IEEE Trans. Ind. Appl.*, vol. 45, no. 1, pp. 167–178, Jan./Feb. 2010.
[20] T. Ohnuma, S. Doki, and S. Okuma, "Signal injection method without torque ripple based on maximum torque control frame," *IEEJ Trans. Elect. Electron. Eng.*, vol. 8, no. 1, pp. 87–93, Jan. 2013.
[21] Z. Zhu and L. Gong, "Investigation of effectiveness of sensorless operation in carrier-signal-injection-based sensorless-control methods," *IEEE Trans. Ind. Electron.*, vol. 58, no. 8, pp. 3431–3439, Aug. 2011.
[22] T. Yoon, J. Lee, and K. Lee, "Rotor position estimation method of IPMSM using HF signal injection and sliding-mode controller," *IEEJ Trans. Elect. Electron. Eng.*, vol. 9, no. S1, pp. S56–S63, Oct. 2014.
[23] R. Leidhold, "Position sensorless control of PM synchronous motors based on zero-sequence carrier injection," *IEEE Trans. Ind. Electron.*, vol. 58, no. 12, pp. 5371–5379, Dec. 2011.
[24] S. Ogasawara, and H. Akagi, "An approach to real-time position estimation at zero and low speed for a PM motor based on saliency," *IEEE Trans. Ind. Appl.*, vol. 34, no. 1, pp. 163–168, Jan./Feb. 1998.
[25] S. Ogasawara, and H. Akagi, "Implementation and position control performance of a position-sensorless IPM motor drive system based on magnetic saliency," *IEEE Trans. Ind. Appl.*, vol. 34, no. 4, pp. 806–812, Jul./Aug. 1998.
[26] M. Gu, S. Ogasawara, and M. Takemoto, "Sensorless IPMSM position estimation based on multi SVPWM with elimination of inverter nonlinear effects," *IEEJ Trans. Elect. Electron. Eng.*, vol. 9, no. 2, pp. 219–227, Mar. 2014.
[27] M. Gu, S. Ogasawara, and M. Takemoto, "A novel magnet polarity identification method for initial position estimation for sensorless IPMSM drive," *IEEJ Trans. Elect. Electron. Eng.*, vol. 9, no. 4, pp. 434–441, Jul. 2014.
[28] Q. Gao, G. Asher, M. Sumner, and P. Makys, "Position estimation of AC machines over a wide frequency range based on space vector PWM excitation," *IEEE Trans. Ind. Appl.*, vol. 43, no. 4, pp. 1001–1010, Jul./Aug. 2007.
[29] E. Robeischl and M. Schroedl, "Optimized INFORM measurement sequence for sensorless PM synchronous motor drives with respect to minimum current distortion," *IEEE Trans. Ind. Appl.*, vol. 40, no. 2, pp. 591–598, Mar./Apr. 2004.
[30] S. Ogasawara, H. Akagi, and A. Nabae, "A novel PWM scheme of voltage source inverters based on space vector theory," in *Proc. Eur. Power Electron. Conf.*, Aachen, Germany, 1989, pp. 1197–1202.
[31] G. Narayanan, D. Zhao, H. K. Krishnamurthy, R. Ayyanar, and V. T. Ranganathan, "Space vector based hybrid PWM techniques for reduced current ripple," *IEEE Trans. Ind. Electron.*, vol. 55, no. 4, pp. 1614–1627, Apr. 2008.
[32] Y. Hua, M.Sumner, G. Asher, Q. Gao, and K. Saleh, "Improved sensorless control of a permanent magnet machine using fundamental pulse width modulation excitation," *IET Electr. Power Appl.*, vol. 5, no. 4, pp. 359–370, Apr. 2011.
[33] M. Gu, S. Ogasawara, and M. Takemoto, "An inductance estimation method for sensorless IPMSM drives based on multiphase SVPWM," in *Proc. Future Energy Electron. Conf.*, 2013, pp. 646–651.

Minglei Gu was born in Wuhan, China, in 1983. He received the B.S. and M.S. degrees in electrical engineering from Huazhong University of Science and Technology, Wuhan, China, in 2005, and 2007, respectively, and the Ph.D. degree in electrical engineering from Hokkaido University, Sapporo, Japan, in 2014.

From 2007 to 2009, he was with Dongfeng Motor Corporation, Wuhan, as a Research Engineer working to develop ac motor drive systems. From 2009 to 2010, he was with the Huazhong University of Science & Technology as a Ph.D. candidate. His research interests include ac motor drive systems and static power converters.

He is a Member of the Institute of Electrical Engineers of Japan.

Satoshi Ogasawara (A'87–M'93–SM'97) was born in Kagawa, Japan, in 1958. He received the B.S., M.S., and Dr. Eng. degrees in electrical engineering from the Nagaoka University of Technology, Niigata, Japan, in 1981, 1983, and 1990, respectively.

From 1983 to 1992, he was a Research Associate with the Nagaoka University of Technology. From 1992 to 2003, he has with the Department of Electrical Engineering, Okayama University, Okayama, Japan. From 2003 to 2007, he was with the Department of Electrical Engineering, Utsunomiya University, Utsunomiya, Japan. Since 2007, he has been a Professor in Graduate School of Information Science and Technology, Hokkaido University, Sapporo, Japan. His research interests include ac motor drive systems and static power converters.

Dr. Ogasawara received the IEEE/PELS Society Prize Paper Award in 1999, and the IEEE/IAS Committee Prize Paper Awards in 1996, 1997, 2003, and 2010. He is a Senior Member of the Institute of Electrical Engineers of Japan.

Masatsugu Takemoto (M'99) was born in Tokyo, Japan, in 1972. He received the B.S. and M.S. degrees in electrical engineering from the Tokyo University of Science, Tokyo, Japan, in 1997 and 1999, respectively, and the Ph.D. degree in electrical engineering from the Tokyo Institute of Technology, Tokyo, in 2005.

In 1999, he joined the Tokyo Institute of Technology, as a Research Associate in the Department of Electrical Engineering. In 2004, he joined the Musashi Institute of Technology, Tokyo, as a Research Associate in the Department of Mechanical Systems Engineering. From 2005, he was a Lecturer. In 2008, he joined the Hokkaido University, Hokkaido, Japan, where he is an Associate Professor with Division of Systems Science and Informatics. He is involved in research on bearingless motors, permanent magnet synchronous motors, axial gap motors, and rare-earth-free motors.

Dr. Takemoto is a Member of the Institute of Electrical Engineers of Japan (IEEJ). He received the IEEJ Transaction Paper Award in 2005 and the First Prize Paper Award from the Electric Machines Committee of the IEEE Industry Applications Society (IAS) in 2011. He served as the Secretary, Vice-Chair, and Chair of the IEEE IAS Japan chapter in 2008–2009, 2010–2011, and 2012–2013.